

# Nuclear resonance reflectivity from a $[^{57}\text{Fe}/\text{Cr}]_{30}$ multilayer with the Synchrotron Mössbauer Source

Marina A. Andreeva,<sup>a,\*</sup> Roman A. Baulin,<sup>a</sup> Aleksandr I. Chumakov,<sup>b,c</sup>  
Rudolf Ruffer,<sup>b</sup> Gennadii V. Smirnov,<sup>c</sup> Yurii A. Babanov,<sup>d</sup>  
Denis I. Devyaterikov,<sup>d</sup> Mikhail A. Milyaev,<sup>d</sup> Dmitrii A. Ponomarev,<sup>d</sup>  
Lazar N. Romashev<sup>d</sup> and Vladimir V. Ustinov<sup>d,e</sup>

Received 7 July 2017

Accepted 29 November 2017

Edited by V. Favre-Nicolin, CEA and  
Université Joseph Fourier, France

**Keywords:** magnetic multilayers; antiferromagnetic interlayer coupling; Mössbauer spectroscopy; nuclear resonance reflectivity; Synchrotron Mössbauer Source.

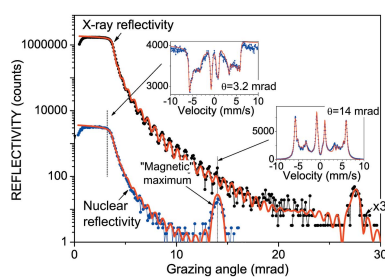
<sup>a</sup>Faculty of Physics, M. V. Lomonosov Moscow State University, Moscow 119991, Russian Federation, <sup>b</sup>ESRF – The European Synchrotron, CS 40220, 38043 Grenoble Cedex 9, France, <sup>c</sup>National Research Centre ‘Kurchatov Institute’, Pl. Kurchatova 1, Moscow 123182, Russian Federation, <sup>d</sup>M. N. Mikheev Institute of Metal Physics UB RAS, Ekaterinburg 620990, Russian Federation, and <sup>e</sup>Institute of Natural Sciences, Ural Federal University, Ekaterinburg 620083, Russian Federation. \*Correspondence e-mail: mandreeva1@yandex.ru

Mössbauer reflectivity spectra and nuclear resonance reflectivity (NRR) curves have been measured using the Synchrotron Mössbauer Source (SMS) for a  $[^{57}\text{Fe}/\text{Cr}]_{30}$  periodic multilayer, characterized by the antiferromagnetic interlayer coupling between adjacent  $^{57}\text{Fe}$  layers. Specific features of the Mössbauer reflectivity spectra measured with  $\pi$ -polarized radiation of the SMS near the critical angle and at the ‘magnetic’ maximum on the NRR curve are analyzed. The variation of the ratio of lines in the Mössbauer reflectivity spectra and the change of the intensity of the ‘magnetic’ maximum under an applied external field has been used to reveal the transformation of the magnetic alignment in the investigated multilayer.

## 1. Introduction

Recently, nuclear resonance experiments with synchrotron radiation (SR) have become an important development due to the implementation of synchrotron Mössbauer sources (SMS) (Smirnov *et al.*, 1997; Smirnov, 2000; Mitsui *et al.*, 2007, 2009; Potapkin *et al.*, 2012). Previously, the time-domain analog of traditional Mössbauer spectroscopy was used at synchrotron stations utilizing the time-resolved signal of nuclear resonant scattering: nuclei excited by a short synchrotron pulse ( $<1$  ns) decay with an essential delay relative to the prompt X-ray scattering. Hyperfine splitting of the nuclear levels is exhibited in time-domain spectroscopy by so-called quantum beats (Trammell & Hannon, 1978; Ruffer *et al.*, 1991; Sturhahn & Gerdau, 1994; Smirnov, 1999). Until recently, this time evolution was the only possible way to register nuclear resonant excitations.

Despite the very complicated method of hyperfine field extraction, time-domain measurements have some advantages over common energy-domain Mössbauer spectroscopy, such as, for example, shorter acquisition times, higher accuracy in the determination of hyperfine parameters (the frequency of the quantum beats can be determined more precisely) and the feasibility for many isotopes where radioactive sources are not commercially (or even fundamentally) available. However, the interpretation of the time spectra is rather complicated and is straightforward only for the simplest hyperfine structures. In time-domain studies, the observable time evolution of



scattered radiation results from coherent interference of radiation scattered *via* various hyperfine transitions. Hyperfine splittings are determined mainly by the interference terms, where each component does not contribute additively. Under these conditions, correct interpretation is possible only for relatively simple systems, and/or if the model of the hyperfine structure is known *a priori*. For more elaborate systems, measurements of Mössbauer spectra on the conventional energy scale, which are now available with SMS, give a clearer picture of the hyperfine interactions. For instance, SMS studies of Fe,Al-bearing silicate perovskite (Kupenko *et al.*, 2015) have allowed for essential refinement of the preliminary model obtained from nuclear forward-scattering (NFS) measurements (Kupenko *et al.*, 2014). Furthermore, SMS investigations of magnesium silicate perovskite revealed that Fe<sup>3+</sup> ions do not undergo a high-spin to low-spin transition, as has been suggested from NFS measurements (Catalli *et al.*, 2010), but remain in the high-spin state in lower-mantle perovskite at conditions throughout the lower mantle (Potapkin *et al.*, 2013).

Different from a common radioactive source, the radiation coming from the SMS is in a needle-like collimated beam of small ( $\sim$ mm) size, which can be further focused to spot sizes of a few micrometers (Potapkin *et al.*, 2012). These properties make the SMS an ideal device for Mössbauer spectroscopy of iron-containing surfaces, thin films and multilayers in grazing geometry when the angular resolution is important. The application of SMS to different types of experiments [some of them are described by Potapkin *et al.* (2012)] has some specific features because the radiation from SMS is fully  $\pi$ -polarized: the electric field vector is in the vertical direction and the magnetic field vector of the radiation is in the horizontal direction. The case of the  $\sigma$ -polarization of SR has been well described for time-domain experiments performed without SMS with natural  $\sigma$ -polarization of the synchrotron beam (Siddons *et al.*, 1993, 1999; Smirnov, 1999; Andreeva, 2001; Röhlberger *et al.*, 2003). The case of  $\pi$ -polarized radiation was not analyzed in detail. The selection rules for nuclear transitions between magnetic hyperfine sublevels lead to a specific line ratio in the Mössbauer spectra and its angular dependence, different for the cases of  $\sigma$ - and  $\pi$ -polarized incident radiation. It is worthwhile noting that in reflectivity spectra the lines are characterized by a peculiar shape, considerably changing with grazing angle variation (Bernstein & Campbell, 1963; Isaenko *et al.*, 1994). This adds a complexity to the correct interpretation of the Mössbauer reflectivity spectra. However, these spectra contain rich depth-selective information about magnetization profiles which should be extracted in the correct way.

In this work we analyze the specific features of the Mössbauer reflectivity spectra, measured using  $\pi$ -polarized radiation from the Synchrotron Mössbauer Source at the ESRF, and demonstrate how a joint fit of the nuclear resonance reflectivity (NRR) curve and the Mössbauer reflectivity spectra measured at several grazing angles exposes the magnetization depth profile in the periodic [<sup>57</sup>Fe/Cr]<sub>30</sub> multilayer and its evolution under an applied field.

## 2. Experiment

A series of Al<sub>2</sub>O<sub>3</sub>/Cr(7 nm)/[<sup>57</sup>Fe(*x* nm)/Cr(*y* nm)]<sub>30</sub>/Cr(1.2 nm) samples with ultrathin Fe layers (0.08 nm < *x* < 0.8 nm) and different Cr spacers (the nominal values are *y* = 1.05 nm and 2.0 nm) were grown with a Katun-C molecular beam epitaxy facility, equipped by five thermal evaporators at the Institute of Metal Physics (Ekaterinburg, Russia). The Fe layers were deposited using an iron target with  $\sim$ 95% enrichment in the <sup>57</sup>Fe isotope, which greatly facilitate the Mössbauer reflectivity investigations. The growth was performed in the UHV regime ( $5 \times 10^{-10}$  mbar). The Fe/Cr multilayers were deposited on the 7 nm-thick Cr buffer layer. During the buffer layer deposition the Al<sub>2</sub>O<sub>3</sub> substrate temperature was gradually decreased from 300°C down to 180°C. The samples were capped with a 1.2 nm-thick Cr layer to prevent oxidation. The typical deposition rate of the Cr and <sup>57</sup>Fe layers was  $\sim$ 0.15 nm min<sup>-1</sup>. The samples were assigned for studying their magnetic properties and Kondo-like behavior (Ustinov *et al.*, 2006; Drovosekov *et al.*, 2008). For example, 1.05 nm Cr spacers have been known to support antiferromagnetic interlayer coupling between <sup>57</sup>Fe layers. In this paper, we present the results obtained for this particular sample with nominal value of the Cr spacers, *y* = 1.05 nm. Results obtained for other samples with the ultrathin <sup>57</sup>Fe layers (less than 0.2 nm), not showing any Bragg peaks in the X-ray and NRR curves, are described elsewhere (Andreeva *et al.*, 2017a,b).

The experiment was performed at the Nuclear Resonance beamline ID18 (Rüffer & Chumakov, 1996) of the ESRF. The storage ring was operated in multi-bunch mode with a nominal storage ring current of 200 mA. The energy bandwidth of the radiation was first reduced down to 2.1 eV by a high-heat-load monochromator (Chumakov *et al.*, 2014) adjusted to the 14.4125 keV energy of the nuclear resonant transition of the <sup>57</sup>Fe isotope. Then X-rays were collimated by compound refractive lenses down to an angular divergence of a few  $\mu$ rad. A high-resolution monochromator (HRM) decreases the energy bandwidth of the beam further to  $\sim$ 15 meV. Final monochromatization down to an energy bandwidth of  $\sim$ 8 neV and a sweep through the energy range of about  $\pm$ 0.5  $\mu$ eV was achieved using the SMS (Smirnov *et al.*, 1997; Smirnov, 2000; Mitsui *et al.*, 2007, 2009; Potapkin *et al.*, 2012). Radiation from the SMS was focused down to a beam size of 8  $\mu$ m  $\times$  10  $\mu$ m using a Kirkpatrick–Baez multilayer mirror system. The intensity of the X-ray beam incident on the sample was  $\sim$ 10<sup>4</sup> photons s<sup>-1</sup>.

The samples were mounted in the cassette holder of the He-exchange gas superconducting cryo-magnetic system and the measurements were performed at helium temperature (4 K) and under a variable external field  $\mathbf{H}^{\text{ext}}$  (0–3 T) applied both along the beam and perpendicular to it in the sample surface plane.

Energy scans across the reflectivity Mössbauer spectra were performed by vibrating the SMS along the beam direction using the Doppler shift method, common in Mössbauer spectroscopy. The angular dependence of the NRR was

obtained as the integral over the Mössbauer reflectivity spectra at each angle of the incident beam. The limits of integration could be changed depending on the total splitting of the Mössbauer reflectivity spectra for different samples in order to obtain the maximal influence of the nuclear resonant scattering on the total reflected intensity. The integration can be carried out either electronically or by broadening the linewidth of the SMS using small deviations from the nuclear Bragg conditions [an explanation of different adjustments of the SMS is given by Potapkin *et al.* (2012)]. The NRR curves are very important for characterization of the magnetic ordering in multilayers (see, for example, Toellner *et al.*, 1995; Bottyán *et al.*, 1998; Andreeva *et al.*, 1999; Kalska *et al.*, 2001; Lindgren *et al.*, 2001; Röhlberger *et al.*, 2002; Diederich *et al.*, 2007; Couet *et al.*, 2009; Ślęzak *et al.*, 2010; Gupta *et al.*, 2010; Andreeva *et al.*, 2015), because contrary to the X-ray reflectivity curves they are sensitive to the magnetic structure of the multilayers.

The NRR curves measured in the energy-domain approach are rather different from those measured in earlier NRR experiments performed in the time-domain. For the time-domain spectroscopy the angular dependencies of the NRR are acquired using the time gating of the delayed scattering at each angle of incidence. The delayed NRR curves are characterized by the so-called ‘interference peak’ (Baron *et al.*, 1994; Toellner *et al.*, 1995), *i.e.* by the maximum at the critical angle of the total external reflection. The appearance of this peak has been attributed to the ‘interference’ of the nuclear resonant scattering amplitude and the amplitude of scattering by the electron shells. A more accurate explanation of this effect has been suggested using the concept of standing waves, created at instant moments by prompt electronic scattering (Andreeva, 1996; Andreeva & Lindgren, 2002).

For the energy-domain approach, the NRR curves show a common, in X-ray reflectivity experiments, plateau in the region of total external reflection (distorted at small angles by the limited overlap of the sample surface with the beam). This is a general property of Fresnel reflectivity (valid for NRR as well) which tends to 1 when the grazing angle  $\theta$  goes to zero. So at low  $\theta$  the modulations of the reflectivity curve by the resonant absorption or refraction are small. This is the reason why the Fourier transform of the reflectivity amplitude, sensitive only to the variable part of the function, tends to 0 as  $\theta$  goes to zero, and it explains the specific shape of the NRR curve measured in the time-domain experiments. Note that exactly this shape of the reflectivity curves was observed in the first Mössbauer experiment on reflectivity (Bernstein & Campbell, 1963) in which the validity of the Fresnel formalism for the nuclear resonant scattering was tested. The interference of the nuclear resonant and electronic scattering amplitudes is revealed as an asymmetric distortion of the lines in Mössbauer reflectivity spectra mostly pronounced near the critical angle of the total external reflection. The lines in Mössbauer reflectivity spectra appear as dips at angles lower than the critical angle, as dispersive-like curves at the critical angle, and as asymmetric peaks at higher angles (Bernstein &

Campbell, 1963; Irkaev *et al.*, 1993a,b, 1995; Isaenko *et al.*, 1994; Andreeva *et al.*, 1998, 2017a,b).

The main purpose of the present work is the study of the antiferromagnetic interlayer coupling in the  $[^{57}\text{Fe}(0.8\text{ nm})/\text{Cr}(1.05\text{ nm})]_{30}$  multilayer (nominal thicknesses are given) by means of NRR performed for the first time in the energy domain with the SMS and the analysis of the Mössbauer reflectivity spectra measured at different grazing angles with  $\pi$ -polarized radiation from the SMS.

### 3. General description of Mössbauer reflectivity spectra with the SMS

Mössbauer reflectivity experiments (Bernstein & Campbell, 1963) started soon after the discovery of the Mössbauer effect. The dispersive shape of the lines in Mössbauer reflectivity spectra, varying from dips to peaks with the change of incidence angle, was clearly demonstrated and explained using the Fresnel formula and taking into account the interference between the nuclear resonant and electron scattering. The sensitivity to the surface oxidation of  $^{57}\text{Fe}$  film was also registered, and this observation determined the important perspectives of the method for investigating surfaces, films and multilayers. However, the practical application of Mössbauer reflectivity was very limited due to the great loss of intensity by the necessity to collimate the radiation from the radioactive source. Therefore, only a few Mössbauer reflectivity experiments had been performed with radioactive sources (Wagner, 1968; Frost *et al.*, 1985; Andreeva *et al.*, 1991, 1997, 1998; Röhlberger *et al.*, 1993; Isaenko *et al.*, 1994; Irkaev *et al.*, 1995) before synchrotron sources were adjusted to this task.

Time-domain Mössbauer reflectivity experiments at synchrotrons started at 1993 (Chumakov *et al.*, 1993; Baron *et al.*, 1994; Toellner *et al.*, 1995) and the results immediately revealed the advantages of SR. The natural perfect collimation and brightness of SR allowed for measurements of the reflected intensity over a large angular scale. The detection of periodicity in magnetic multilayers (or isotopic periodicity) became possible by observation of the ‘magnetic’ or ‘isotopic’ maxima on the NRR angular curve (Chumakov *et al.*, 1993; Toellner *et al.*, 1995; Deák *et al.*, 1999; Gupta *et al.*, 2005, 2008; Rennhofer *et al.*, 2006; Diederich *et al.*, 2007; Andreeva *et al.*, 2015). The NRR curves were measured using the time gating, *i.e.* by detection of the integral delayed nuclear resonant response after the prompt SR pulse.

The essential issue in SR time-domain NRR is the polarization characteristics of different hyperfine transitions excited by the  $\sigma$ -polarized SR beam. The quantum beats in the time spectrum of the coherent nuclear resonant scattering or reflectivity are the result of the interference of waves re-emitted by selectively excited hyperfine transitions with slightly different photon energies. The polarization of these waves directly determines the resulting beat pattern as has been clearly illustrated, for example, in the review paper of Smirnov (1999).

Polarization properties of the amplitude of the nuclear resonant scattering in the presence of the hyperfine splitting of

nuclear levels make the reflectivity theory much more complicated compared with X-ray reflectivity theory. The  $4 \times 4$ -matrix theory of Mössbauer reflectivity from multilayers (general for the energy and time domains, but developed initially for experiments with radioactive sources in the energy domain) has been developed and presented in many papers (Andreeva & Rosete, 1986; Irkaev *et al.*, 1993b; Röhlberger, 1999; Andreeva *et al.*, 2015). Peculiarities in the reflectivity time spectra, measured with  $\sigma$ -polarized SR for various angles of the incident beam and different hyperfine field arrangements in the multilayer, have been thoroughly analyzed (Chumakov *et al.*, 1999; Röhlberger *et al.*, 2003; Andreeva & Lindgren, 2005; Andreeva *et al.*, 2007). Specific patterns of the reflectivity time spectra at various grazing angles and Bragg maxima of the reflectivity from periodic multilayers have been effectively used for the description of the magnetization depth-profiles in the investigated samples (see, for example, Röhlberger *et al.*, 2003; Ślęzak *et al.*, 2010; Andreeva *et al.*, 2015). For the data analysis the program package *REFTIM* has been developed and uploaded to the ESRF scientific software web site (Andreeva, 2008; Andreeva *et al.*, 2016b).

The recent development of SMS at the nuclear resonance beamline ID18 of the ESRF allows for acquiring the conventional energy-domain, *i.e.* Mössbauer reflectivity spectra, which give a more understandable and clear picture of hyperfine interactions. However, Mössbauer reflectivity spectra are quite different from Mössbauer absorption spectra due to the interference nature of the reflectivity process. Furthermore, the reflectivity spectra are measured at grazing incidence angles and they ‘feel’ the magnetization direction in a sample from the other ‘view’ than that in the absorption experiments, usually taken at normal incidence. Moreover, the radiation from a radioactive source is not polarized, but in Mössbauer experiments with the SMS the radiation is  $\pi$ -polarized. Therefore, some new features appear in Mössbauer reflectivity spectra measured with the SMS relative to the experiments with a radioactive source and time-domain nuclear resonance experiments.

The amplitudes of the nuclear resonant scattering in the forward direction, including the change of polarization  $\nu \rightarrow \nu'$ , have the following expression (in the case of the dipole nuclear resonant transitions),

$$f_j^{\text{nucl}}(\omega, \nu \rightarrow \nu') = -\frac{1}{2\lambda} \sigma_{\text{res}} \frac{2L+1}{2I_e+1} f_j^{\text{LM}} \times \sum_{m_e, m_g} \frac{(\Gamma_j/2) | \langle I_g m_g L \Delta m | I_e m_e \rangle |^2}{\hbar\omega - E_{jR}(m_e, m_g) + (i\Gamma_j/2)} \times [\mathbf{h}_{j\Delta m} \circ \mathbf{h}_{j\Delta m}^*]_{\nu \rightarrow \nu'}, \quad (1)$$

where, for  $^{57}\text{Fe}$ ,  $L = 1$ ,  $I_e = 3/2$ ,  $I_g = 1/2$ ,  $m_e, m_g$  are the magnetic quantum numbers,  $\Delta m = m_e - m_g = \pm 1, 0$ ,  $\langle I_g m_g L \Delta m | I_e m_e \rangle$  are the Clebsch–Gordan coefficients,  $\sigma_{\text{res}} = 2.56 \times 10^{-4} \text{ nm}^2$  is the resonant cross section (<http://www.medc.dicp.ac.cn/Resources-isotopes/Resource-Fe.php>),  $\lambda = 0.086 \text{ nm}$ ,  $j$  numerates the kinds of hyperfine splitting (*i.e.* different multiplets in the Mössbauer spectrum),  $f_j^{\text{LM}}$  is the Lamb–

Mössbauer factor, and  $\hat{\mathbf{h}}_{\Delta m}$  in (1) are the spherical orfts in the hyperfine field principal axis  $\mathbf{h}_x, \mathbf{h}_y, \mathbf{h}_z$ ,

$$\mathbf{h}_{\pm 1} = \mp i \frac{\mathbf{h}_x \pm i\mathbf{h}_y}{\sqrt{2}}, \quad \mathbf{h}_0 = i\mathbf{h}_z, \quad (2)$$

and the sign  $\circ$  designates the outer product of these spherical orfts.

In calculating the reflectivity we use the susceptibility of the resonant medium which consists of two parts,

$$\hat{\chi} = \chi^{\text{el}} + \hat{\chi}^{\text{nucl}}(\omega), \quad (3)$$

associated with the scattering by the electrons  $\chi^{\text{el}}$  and by resonant nuclei  $\hat{\chi}^{\text{nucl}}(\omega)$ ,

$$\hat{\chi}^{\text{nucl}}(\omega) = \frac{\lambda^2}{\pi} \sum_j \rho_j^{\text{nucl}} [f_j^{\text{nucl}}(\omega)]_{\nu, \nu'}, \quad (4)$$

where  $\rho_j^{\text{nucl}}$  is the volume density of the resonant nuclei.  $\hat{\chi}^{\text{nucl}}(\omega)$  should be considered as a tensor, determined by the sum of the outer products of the spherical orfts of the hyperfine field principal axis. For the transverse parts of these tensors, presented as the matrices in the  $\sigma$ - and  $\pi$ -polarization orfts (Andreeva & Rosete, 1986; Irkaev *et al.*, 1993b; Röhlberger, 1999; Andreeva *et al.*, 2015), the following expressions can be written

$$\hat{\chi}_{\Delta m=0}^{\perp} \propto \begin{pmatrix} \sin^2 \beta \cos^2 \gamma & -\sin \beta \cos \beta \cos \gamma \\ -\sin \beta \cos \beta \cos \gamma & \cos^2 \beta \end{pmatrix}, \quad (5)$$

$$\hat{\chi}_{\Delta m=\pm 1}^{\perp} \propto \frac{1}{2} \begin{pmatrix} \sin^2 \gamma + \cos^2 \gamma \cos^2 \beta & (\cos \beta \cos \gamma \mp i \sin \gamma) \sin \beta \\ (\cos \beta \cos \gamma \pm i \sin \gamma) \sin \beta & \sin^2 \beta \end{pmatrix}, \quad (6)$$

where  $\beta$  and  $\gamma$  are the polar and azimuth angles describing the orientation of the hyperfine magnetic field  $\mathbf{B}_{\text{hf}}$  relative to the sample surface and the beam direction (Fig. 1). The index  $j$ , specific for each multiplet, in (2)–(6) is omitted for simplicity.

More accurately, the angular dependences of the amplitudes of scattering should be determined for the wavevectors of the incident and reflected beams  $\mathbf{k}_0$  and  $\mathbf{k}_R$ , but in Mössbauer reflectivity experiments the grazing angles  $\theta$  of the incident and reflected beams are so small ( $\theta < 1^\circ$ – $2^\circ$ ) that for

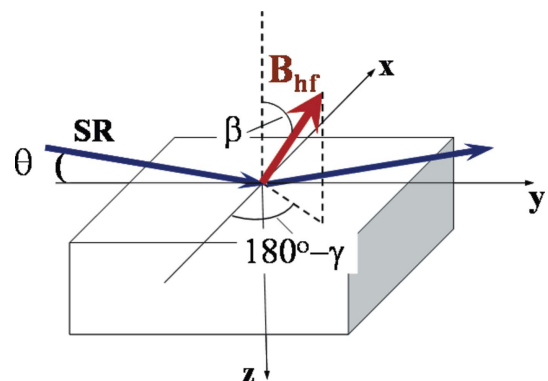


**Figure 1** Coordinate system describing the orientation of the hyperfine magnetic field  $\mathbf{B}_{\text{hf}}$ .

the angular dependences of the scattering amplitudes their difference from the direction along the surface (further we denote the beam direction as  $\mathbf{k}$ ) can be neglected. The special case when the angle  $\theta$  plays a noticeable influence on the angular dependences of the scattering amplitudes in the reflectivity theory has been considered by Andreeva (2010).

For the 14.4 keV M1 nuclear transition in  $^{57}\text{Fe}$  the matrices in equations (5) and (6) should be considered for the magnetic field of radiation which corresponds to the  $\pi$ -,  $\sigma$ -case for  $\sigma$ ,  $\pi$ -polarization of the electric field of radiation. Therefore, the vector-column of the magnetic field of radiation for the  $\pi$ -polarized incident radiation from SMS is represented as

$$\begin{pmatrix} 1 \\ 0 \end{pmatrix},$$

and the first columns in equations (5) and (6) describe the angular dependences and polarization properties of the amplitudes of the nuclear resonant scattering  $f_{\Delta m}^{\text{nucl}}$  in the case of SMS usage.

The total algorithm of the NRR calculations based on the  $4 \times 4$ -propagation matrices is rather lengthy and is not presented here. It is described in many papers (see, for example, Andreeva & Rosete, 1986; Irkaev *et al.*, 1993b; Röhlberger, 1999; Andreeva *et al.*, 2015). The result of the multiple interference of waves reflected by boundaries of each layer and subjected to the polarization transformation is difficult to understand and for a qualitative picture we use the simplest kinematical approximation, strictly applicable at angles two to three times larger than the critical angle, but approximately for all angles [see the detailed description in the paper by Andreeva & Lindgren (2005)].

For the periodic multilayer in which the magnetic period is twice the chemical period  $D$ , the structure amplitude for the magnetic period of the nuclear resonant scattering can be used,

$$F_{\Delta m}^{\text{nucl}} = f_{\Delta m}^{\text{nucl}}(\beta_1, \gamma_1) + f_{\Delta m}^{\text{nucl}}(\beta_2, \gamma_2) \exp(2i\varphi), \quad (7)$$

where  $2\varphi \simeq (4\pi D/\lambda) \sin \theta$ , and  $\lambda$  is the radiation wavelength. The phase difference between the waves reflected by two subsequent magnetic layers in the magnetic period is equal to  $2\varphi = 2\pi, 4\pi$  for the Bragg (structure) maxima on the reflectivity curve (and at the critical angle, where  $2\varphi \simeq 0$ ) and to  $2\varphi = \pi, 3\pi, \dots$  for the 'magnetic' maxima with half-order indexes  $1/2, 3/2$  etc. In the case of the plane antiferromagnetic structure,  $\beta_1 = \beta_2 = \beta = 90^\circ$ . The noncollinear ( $\gamma_2 \neq \gamma_1 + 180^\circ$ ) and collinear ( $\gamma_2 = \gamma_1 + 180^\circ = \gamma$ ) antiferromagnetic alignment between two magnetic layers in the magnetic period gives the polarization dependences of the structure amplitudes for the  $\pi$ -polarized incident radiation presented by the vector columns in Fig. 2. It should be noted that in spite of the fact that the electronic scattering is always included in the total susceptibility (3) for the reflectivity calculations, the polarization dependences of the reflectivity are completely determined by the nuclear resonant scattering because the electronic scattering at grazing angles has no dependence on the polarization (the difference between reflectivity for  $\sigma$ - and

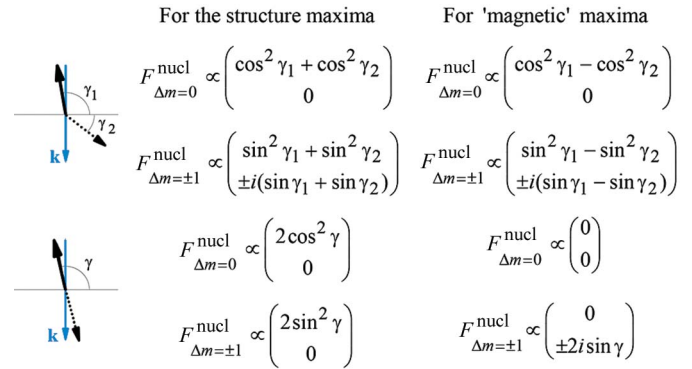


Figure 2

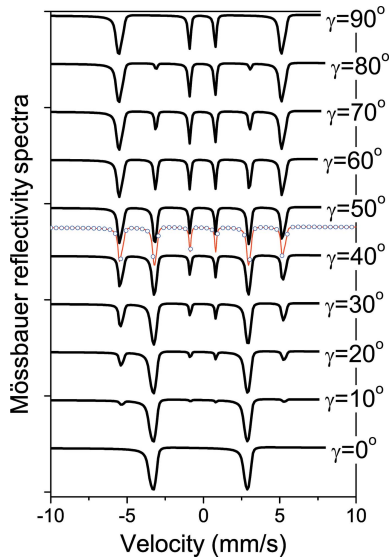
Angular dependences of the vector-column of the structure amplitudes (in  $\pi$ -,  $\sigma$ -orts) for the 'magnetic' period in the case of the noncollinear (top part) and collinear (bottom part) antiferromagnetically coupled magnetic layers in a multilayer for various hyperfine transitions ( $\Delta m = \pm 1, 0$ ) and for the  $\pi$ -polarized incident wave.

$\pi$ -polarization of the incident radiation is negligibly small at grazing angles).

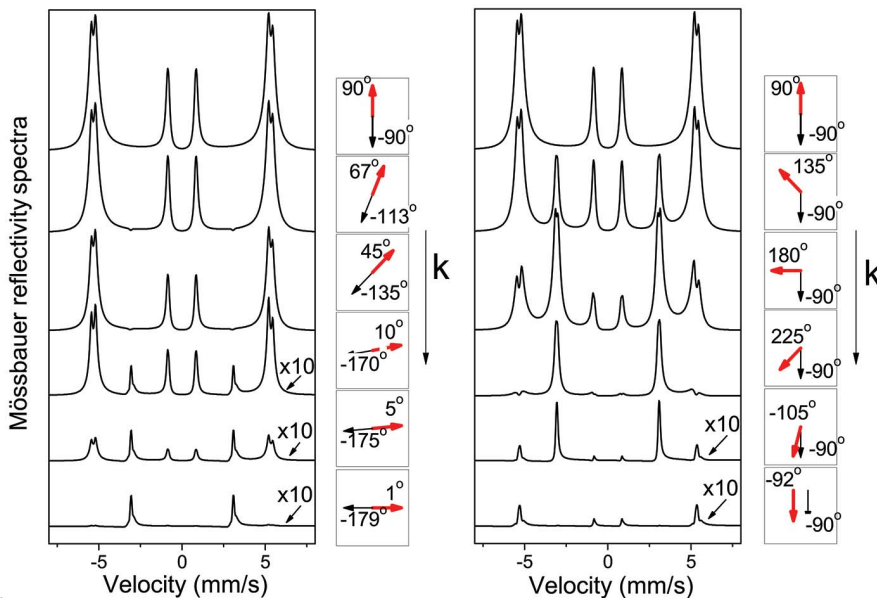
The angular dependences of the different hyperfine lines in the Mössbauer reflectivity spectrum for the case of the antiferromagnetic interlayer coupling determine the specific ratio of lines in the spectra depending on the orientation of the direction of the antiferromagnetic alignment relative to the beam direction. These variations of the spectrum shape are illustrated in Figs. 3 and 4. Note that the spectra at the angles below the critical angle of the total external reflection (Fig. 3) are similar to the absorption spectra (dips near the resonant energies), because the reflectivity in the region of the total reflection is smaller for the larger absorption associated with resonances. The slight asymmetry of these spectra is explained by the interference with the electronic scattering and refraction effect [which is mostly pronounced at the critical angle (Bernstein & Campbell, 1963)]. The spectra in the 'magnetic' maximum, which has an almost pure nuclear origin, look like the emission spectra (Fig. 4); however, the refraction effects as well can also cause their asymmetric distortion (Andreeva *et al.*, 2016a).

Fig. 2 shows that for the collinear antiferromagnetic structure the polarization of the reflected beam in the structure maxima is the same as the polarizations of the incident beam. When the orientation of the magnetization and correspondingly the hyperfine fields  $\mathbf{B}_{\text{hf}}^{(i)}$  of the two antiferromagnetically coupled layers ( $i = 1, 2$ ) are perpendicular to the SR beam ( $\gamma = 0$ ), only the second and fifth lines with  $\Delta m = 0$  are presented in the Mössbauer reflectivity spectrum. When  $\mathbf{B}_{\text{hf}}^{1,2}$  are along the SR beam ( $\gamma = \pm 90^\circ$ ), the four lines with  $\Delta m = \pm 1$  (the first, third, fourth and sixth lines) appear in the Mössbauer reflectivity spectrum (see Fig. 3). Calculations presented in Fig. 3 have been performed for a [ $^{57}\text{Fe}(0.8 \text{ nm})/\text{Cr}(1.05 \text{ nm})$ ] $_{30}$  multilayer, the value of the magnetic hyperfine field  $|\mathbf{B}_{\text{hf}}^{1,2}|$  is taken equal to 33 T with 1.0 T field distribution. So the cases of the  $\pi$ - and  $\sigma$ -polarizations of the incident radiation are rather different. In the previous synchrotron nuclear resonance experiments when the  $\sigma$ -polarized incident radiation was used (without the SMS), the second and fifth

lines were absent at any azimuth orientation of magnetization in the surface plane. In the case of the  $\pi$ -polarized incident radiation the relative intensity of the lines directly determines the azimuth of the  $\mathbf{B}_{\text{hf}}^{(i)}$  alignment.



**Figure 3** Mössbauer reflectivity spectra at grazing-incidence angle  $\theta = 3$  mrad (slightly below the critical angle of the total external reflection), calculated for the  $[^{57}\text{Fe}(0.8 \text{ nm})/\text{Cr}(1.05 \text{ nm})]_{30}$  multilayer characterized by the collinear antiferromagnetic alignment between  $^{57}\text{Fe}$  layers. The spectra are calculated assuming  $\pi$ -polarization of the incident radiation for the  $\mathbf{B}_{\text{hf}}^{1,2}$  orientation in the surface plane ( $\beta = 90^\circ$ ) and various azimuth angles  $\gamma$ . The red curve, marked by the blue circles, shows the spectrum for the randomly distributed orientation of the antiferromagnetically coupled  $\mathbf{B}_{\text{hf}}^{1,2}$  in the surface plane. For clarity, the subsequent spectra are shifted vertically.



**Figure 4** Calculated Mössbauer reflectivity spectra at the ‘magnetic’ maximum ( $\theta = 12.2$  mrad) for the  $[^{57}\text{Fe}(0.8 \text{ nm})/\text{Cr}(1.05 \text{ nm})]_{30}$  multilayer. The spectra are calculated for  $\pi$ -polarization of the incident radiation, and for various orientations of the hyperfine magnetic fields  $\mathbf{B}_{\text{hf}}^{1,2}$  in the surface plane, shown by the pictograms near each spectrum. The spectra for the collinear antiferromagnetic coupling are on the left, and those for the noncollinear coupling are on the right panel. The spectra at the bottom of both panels correspond to the almost vanished intensity of the ‘magnetic’ maximum. The curves are vertically shifted for clarity.

For collinear antiferromagnetic structure the structure amplitudes at the ‘magnetic’ maxima differ from zero only for  $\Delta m = \pm 1$  transitions and only the radiation with the ‘rotated’ polarization contributes to these maxima. It is clearly seen from Figs. 2 and 4 that the intensity of the ‘magnetic’ maxima is maximal when  $\gamma = \pm 90^\circ$ , but if  $\gamma = 0^\circ, 180^\circ$  then the ‘magnetic’ maxima are practically absent. The appearance of the second and fifth lines in the Mössbauer reflectivity spectra measured at the ‘magnetic’ maximum should be evidence of the noncollinear antiferromagnetic structure (Fig. 4). However, these two lines always have the same polarization as the polarization of the incident beam (*i.e.*  $\pi$ -polarization).

The exact calculation does not give the absolute absence of the second and fifth lines when magnetizations are almost perpendicular to the beam direction (*e.g.* for  $\gamma_1 = 1^\circ, \gamma_2 = 180^\circ$ ), because the  $2\varphi = \pi, 3\pi$  phase condition for the ‘magnetic’ maxima is too idealized. The phase shift for the wave reflected from the second layer relative to the amplitude of scattering by the first layer in the magnetic period should be calculated by the exact formula (here we neglect the buffer nonresonant layer for simplicity),

$$2\varphi = (4\pi/\lambda) \eta_1 d_1, \quad (8)$$

where

$$\eta_1 = (\sin^2 \theta + \chi_1)^{1/2} \simeq \sin \theta + \frac{\chi_1}{2 \sin \theta}. \quad (9)$$

This expression includes the refraction and absorption in the first resonant layer with thickness  $d_1$  and susceptibility  $\chi_1$ . Let us evaluate how significant can be the decrease of the amplitude of scattering returned from the second layer due to the absorption in the first layer at grazing angles,

$$|\exp(2i\varphi)| \simeq \exp \left\{ -\frac{4\pi}{\lambda} \frac{\text{Im} \chi_1}{2 \sin \theta} d_1 \right\}. \quad (10)$$

For  $d_1 = 10 \text{ \AA}$ ,  $\theta = 10$  mrad,  $\lambda = 0.86 \text{ \AA}$  and  $\text{Im} \chi \simeq 10^{-5}$  (evaluated in resonance for  $^{57}\text{Fe}$ ), we obtain the value  $\exp(-0.073) \simeq 0.93$ . This means that the amplitudes of scattering by the first and second layers are not equal and when they are added in antiphase at the magnetic maximum they do not compensate each other. So the total suppression of the  $\pi \Rightarrow \pi$  component of the  $F_{\Delta m=0}^{\text{nucl}}$  and  $F_{\Delta m=\pm 1}^{\text{nucl}}$  structure amplitudes in the ‘magnetic’ maxima for the collinear antiferromagnetic case does not take place. This contribution is small but noticeable if the main contribution of the  $\pi \Rightarrow \sigma$  component of  $F_{\Delta m=\pm 1}^{\text{nucl}}$  is small and the intensity of the magnetic maximum becomes very low (see, for example, the spectra at the bottom of Fig. 4).

The refraction and absorption effects in one resonant layer appeared in the difference of the Mössbauer reflectivity spectra calculated for the reversed sequence of the layers with nonsymmetrical angles of the  $\mathbf{B}_{\text{hf}}^{1,2}$  orientation in a magnetic period (Fig. 5). The electronic contributions to the total reflectivity from nonresonant top or bottom layers could also essentially disturb the shape of the Mössbauer reflectivity spectra. In real experiments, the hyperfine field values have a broad distribution (as usual for thin  $^{57}\text{Fe}$  layers when the interfaces are comparable with the layer thickness). The line overlap, the refraction and absorption effects have an essential influence on the shape of the Mössbauer reflectivity spectra. In addition to that, this shape substantially depends on the slight variation of the angle in the vicinity of the critical or Bragg angles (see, for example, Andreeva *et al.*, 2016a).

The next important question is what we shall observe in the case of the multi-domain sample. The result strongly depends on the transverse coherence length of the incident radiation (Baron *et al.*, 1996; Baron, 1999), which for grazing incidence has to be re-evaluated for the direction along the surface. For example, if the transverse coherence of the beam is  $\sim 3\ \mu\text{m}$ , then at a  $\sim 10\ \text{mrad}$  grazing angle the condition of coherent scattering spreads over  $\sim 300\ \mu\text{m}$  distance along the surface. The typical size of the magnetic domains is several micrometers. Therefore, coherent averaging over various domains can take place.

For the angular dependences, presented in Fig. 2, the averaging over various domains (in which the antiferromagnetic coupling of layers over depth takes place) will not be complicated. For the structure maxima, if the lines in the Mössbauer reflectivity spectrum are not overlapped, then the coherent and the incoherent averaging of the reflectivity spectra over the surface plane for the case of the random orientations of the domain magnetizations give the same ratio of lines. This is because the mean values of  $\sin^2\gamma$  and  $\cos^2\gamma$  or  $\sin^4\gamma$  and  $\cos^4\gamma$  are the same (1/2 and 3/8, respectively). The spectrum shape for the domains with randomly orientated

magnetizations is shown in Fig. 3. Obviously the same ratio of lines in the magnetic sextet takes place at  $\gamma \simeq 45^\circ$ . (The exact calculations with the refraction and absorption corrections gives  $\gamma^{\text{eff}} \simeq 47.4^\circ$  for the random in plane  $\mathbf{B}_{\text{hf}}^{1,2}$  orientations and  $\gamma^{\text{eff}} \simeq 55.7^\circ$  for the random in space  $\mathbf{B}_{\text{hf}}^{1,2}$  orientations.)

For the ‘magnetic’ maxima, the coherent averaging of the reflectivity amplitudes over the surface plane at the random orientations of the domains completely destructs the ‘magnetic’ maxima for the case of the collinear antiferromagnetic ordering (because  $\sin\gamma = 0$ ). The incoherent averaging of the reflectivity intensity over various domains with random orientations leads to the intensity of the ‘magnetic’ maximum equal to half of the reflectivity intensity from a single domain sample with  $\gamma = 90^\circ$ , because  $\sin^2\gamma = 1/2$ . Therefore, the relative intensities of the diffraction maxima on the NRR curve helps to eliminate the uncertainties in the magnetic structure determinations.

It can be easily understood that practically any ratio of lines in a Mössbauer reflectivity spectrum measured at only one grazing angle can be interpreted in two ways: as (i) the existence of a single magnetic domain with specific azimuth orientation of magnetizations, and (ii) the partially coherent scattering by a multidomain surface with some preferred orientation of magnetizations. In most cases, the azimuth angle  $\gamma$  obtained by the fit to the spectrum should be considered as the ‘effective’ azimuth angle  $\gamma^{\text{eff}}$ . The measurements at various maxima on the reflectivity curve and at different orientations of the sample can help in the true interpretation of the Mössbauer reflectivity spectra.

The presented, even though simplified, description of the basic properties of the Mössbauer reflectivity spectra for  $\pi$ -polarized incident radiation from SMS nevertheless shows that the method can be effectively used for revealing the magnetic structure in multilayers.

#### 4. Experimental data

The sample  $\text{Al}_2\text{O}_3/\text{Cr}(7\ \text{nm})/[\text{Fe}(0.8\ \text{nm})/\text{Cr}(1.05\ \text{nm})]_{30}/\text{Cr}(1.2\ \text{nm})$  (the nominal thicknesses of the layers are given) has been chosen as the best candidate for demonstrating the peculiarities of the NRR (Mössbauer reflectometry) method, performed with the SMS in the conventional energy scale.

The NRR angular curve, measured with SMS as the integral over the Mössbauer reflectivity spectra at each angle of the incident beam, has shown the existence of the ‘magnetic’ maximum of rather high intensity (Fig. 6), indicating that the magnetic period is twice the chemical period  $D$ . The Mössbauer reflectivity spectra have been measured not only near the critical angle of total external reflection but at the ‘magnetic’ maximum as well. The different shape of these two spectra is clearly seen in Fig. 6.

The presence of the ‘magnetic’ maximum in the NRR curve for zero  $\mathbf{H}^{\text{ext}}$ , when one cannot expect the initial single-domain case with definite direction of the antiferromagnetic alignment, has been explained in the previous section as the result of the incoherent averaging of the reflectivity over various domains. It has been concluded that for the equiprobable

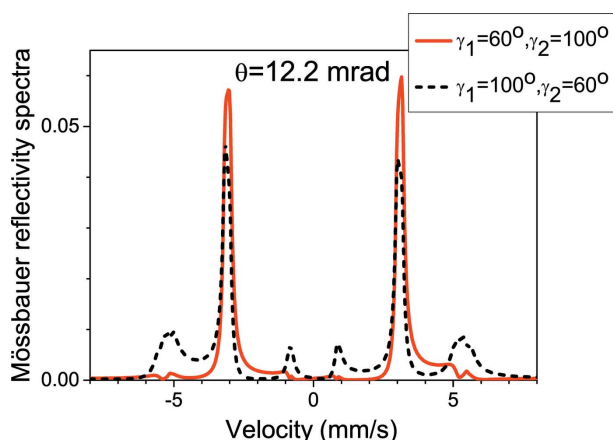


**Figure 5** Comparison of the Mössbauer reflectivity spectra at the ‘magnetic’ maximum calculated for different sequences of the magnetization orientations in the two  $^{57}\text{Fe}$  layers:  $\gamma_1$  refers to the upper layer,  $\gamma_2$  refers to the lower layer in the magnetic period. Calculations are performed with the same parameters of the structure as taken for Fig. 4.

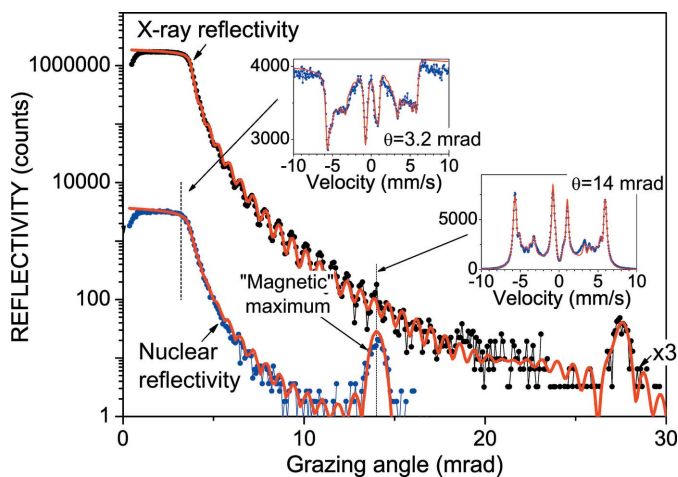


**Figure 6** X-ray (for  $\lambda = 0.086$  nm) and NRR curves measured in the absence of an external magnetic field ( $\mathbf{H}^{\text{ext}} = 0$ ). In the insets are Mössbauer reflectivity spectra, measured slightly below the critical angle of total external reflection and at the ‘magnetic’ maximum. Symbols are the experimental data; the lines show fits.

orientations of magnetizations in magnetic domains we should obtain the effective angle  $\gamma \simeq 45^\circ$ . However, the joint fit of the nuclear reflectivity curve and Mössbauer reflectivity spectra measured near the critical angle and at the ‘magnetic’ maximum gives the effective azimuth angle  $\gamma \simeq 66^\circ$ . This means that, even at remanence, the sample still keeps some preferred orientation of the magnetization in various domains along the longer side of the sample. (The sample has surface dimensions of  $\sim 5$  mm  $\times$  15 mm and the longer side has been oriented along the beam).

The changes of the ‘magnetic’ maximum in the NRR curve (Fig. 7) and of the Mössbauer reflectivity spectra (Fig. 8) characterize the reorientation of the antiferromagnetic alignment in the adjacent  $^{57}\text{Fe}$  layers under the applied field  $\mathbf{H}^{\text{ext}}$ , as shown by the pictograms in Figs. 7 and 8. For the rather small field of  $\sim 0.15$  T, the ‘magnetic’ maximum disappears if  $\mathbf{H}^{\text{ext}}$  is parallel to the beam ( $\mathbf{k}$  direction), and one could suppose that the antiferromagnetic ordering has already collapsed into ferromagnetic alignment. But the additional measurements with  $\mathbf{H}^{\text{ext}}$  perpendicular to the beam show the highest intensity of the ‘magnetic’ maximum. This is direct evidence of the spin-flop transition: the antiferromagnetically coupled, in the adjacent  $^{57}\text{Fe}$  layers, hyperfine fields  $\mathbf{B}_{\text{hf}}^{(i)}$  rotate perpendicular to  $\mathbf{H}^{\text{ext}}$ . According to Fig. 2, if  $\mathbf{B}_{\text{hf}}^{(i)} \perp \mathbf{H}^{\text{ext}} \parallel \mathbf{k}$  ( $\gamma_1 = 0, \gamma_2 = 180^\circ$  or *vice versa*), the ‘magnetic’ maximum disappears because the projections of  $\mathbf{B}_{\text{hf}}^{(i)}$  on the beam direction become equal. But, if  $\mathbf{B}_{\text{hf}}^{(i)} \perp \mathbf{H}^{\text{ext}} \perp \mathbf{k}$  ( $\gamma_1 = 90^\circ, \gamma_2 = -90^\circ$  or *vice versa*),

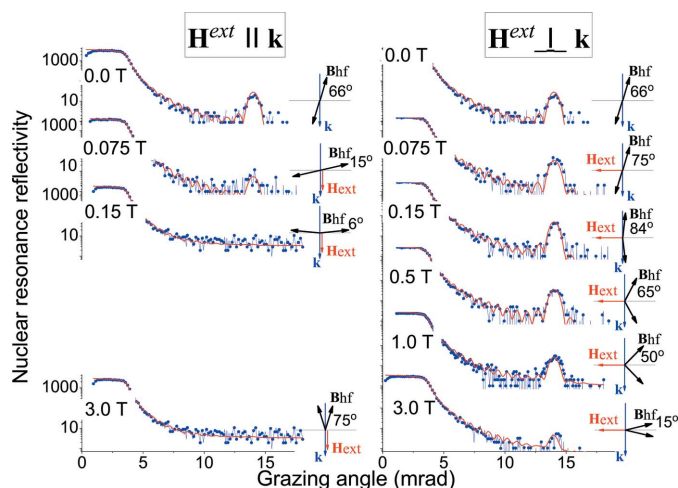


**Figure 7** NRR curves measured for various values and orientations of the external magnetic field  $\mathbf{H}^{\text{ext}}$ . The pictograms near each curve show the orientation of the hyperfine fields  $\mathbf{B}_{\text{hf}}^{1,2}$  in the adjacent  $^{57}\text{Fe}$  layers derived from the fit.

the difference of the projections of  $\mathbf{B}_{\text{hf}}^{(i)}$  on the beam direction for two  $^{57}\text{Fe}$  layers in the magnetic period are the largest, and the ‘magnetic’ maximum has the maximal intensity. Notice that at the maximal  $\mathbf{H}^{\text{ext}} = 3$  T, applied perpendicular to the beam, the ‘magnetic’ maximum still exists. Therefore, even with  $\mathbf{H}^{\text{ext}}$  as high as 3 T the complete ferromagnetic alignment is still not attained.

The fit of the NRR curves (Fig. 7) has been performed jointly with the fit of the Mössbauer reflectivity spectra [Figs. 8(a) and 8(b)]. The program package *REFTIM* has been modified to *REFSPC* specifically for these studies (Andreeva *et al.*, 2016b). The spin-flop state at  $\mathbf{H}^{\text{ext}} = 0.15$  T reveals itself in the case of  $\mathbf{H}^{\text{ext}} \parallel \mathbf{k}$  by the presence of only the second and fifth lines in the Mössbauer reflectivity spectra, measured near the critical angle of total external reflection (Fig. 8a). The similar ‘two’ lines spectrum appears when  $\mathbf{H}^{\text{ext}}$  is perpendicular to the scattering plane but only at an external field of 3 T.

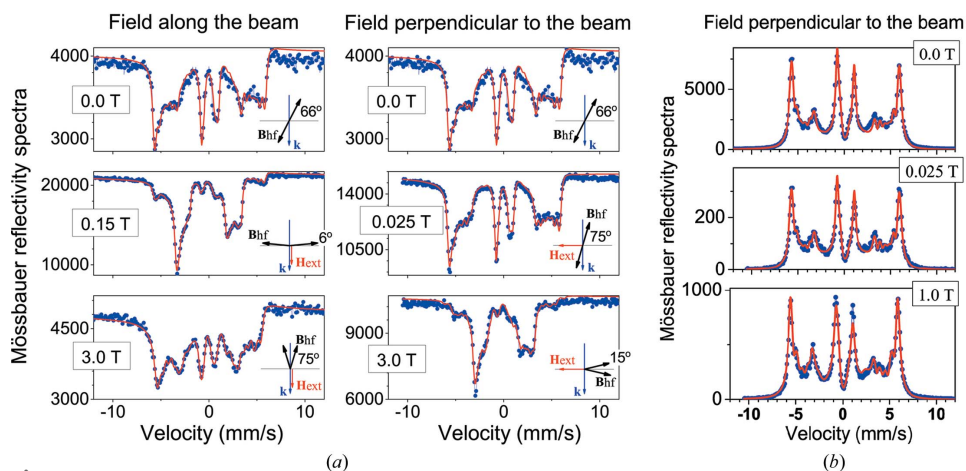


**Figure 8** Mössbauer reflectivity spectra measured slightly below the critical angle of total external reflection (a) and at the ‘magnetic’ maximum (b) for various values and orientations of the external magnetic field  $\mathbf{H}^{\text{ext}}$ . Symbols show the experimental data, the lines show the fit. The pictograms have the same meaning as in Fig. 7.

This means that in this case  $\mathbf{B}_{\text{hf}}^{(i)}$  are aligned almost completely ferromagnetically (and antiparallel to  $\mathbf{H}^{\text{ext}} \perp \mathbf{k}$ ) as presented by the pictograms in Figs. 7, 8(a) and 8(b). Truthfully speaking, during the fit we exclude from the sequence of the repeated layers the first and bottom bilayer which always have slightly different structure and magnetic orientation parameters.

The spectra in Figs. 8(a) and 8(b) are fitted with seven values of  $\mathbf{B}_{\text{hf}}^{(i)}$  with some field distribution  $\Delta\mathbf{B}_{\text{hf}}^{(i)}$  broadening each magnetic sextet. This gives the total field distribution  $P(\mathbf{B}^{\text{tot}})$ , presented in Fig. 9, where  $\mathbf{B}^{\text{tot}} = |\mathbf{H}^{\text{ext}} + \sum_i \mathbf{B}_{\text{hf}}^{(i)}|$  is the total field, acting on the nuclei. The preferred antiparallel alignment of  $\mathbf{B}_{\text{hf}}^{(i)}$  and  $\mathbf{H}^{\text{ext}}$ , typical for  $^{57}\text{Fe}$  nuclei in metals, is shown by the continuous decrease of the position of the maximum in the  $P(\mathbf{B}^{\text{tot}})$  distribution with increasing value of  $\mathbf{H}^{\text{ext}}$ . The broadening of each  $\mathbf{B}_{\text{hf}}^{(i)}$  in the field distribution  $P(\mathbf{B}^{\text{tot}})$  at some intermediate values of the external field, e.g. at  $\mathbf{H}^{\text{ext}} = 1$  T, can be explained by the presence of some angular distributions of the  $\mathbf{B}_{\text{hf}}^{(i)}$  orientation. The influence of the angular distribution of  $\mathbf{B}_{\text{hf}}^{(i)}$  on the smearing of the magnitudes of  $\mathbf{B}^{\text{tot}}$  in  $P(\mathbf{B}^{\text{tot}})$  is illustrated in Fig. 10. This broadening of various components in  $P(\mathbf{B}^{\text{tot}})$  persists up to 3 T as seen in Fig. 9. In fact, the azimuth angles, shown by pictograms in Figs. 7 and 8(a), actually mean some effective angles at which we obtain a relatively good fit of the reflectivity data, but taking into account the broadened angular distribution of different contributions to  $\mathbf{B}^{\text{tot}}$ .

The Mössbauer reflectivity spectra, measured at the ‘magnetic’ maximum (Fig. 8b), have a practically unchanged shape at different values of  $\mathbf{H}^{\text{ext}}$ , at least as far as the ‘magnetic’ maximum still having a reasonable intensity. They are fitted with the same distribution  $P(\mathbf{B}^{\text{tot}})$  and  $\mathbf{B}_{\text{hf}}^{(i)}$  orienta-

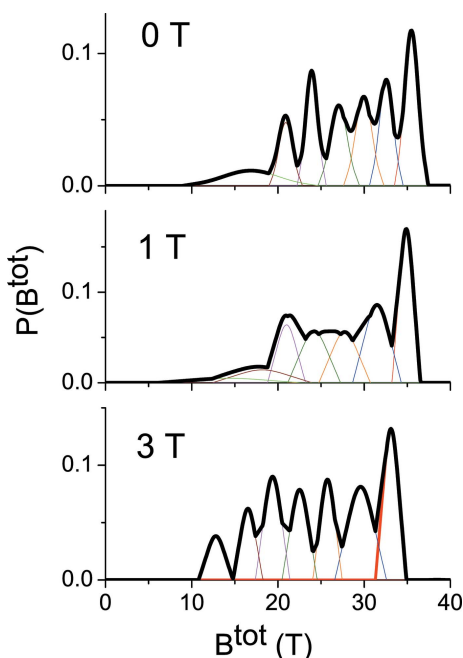


Figure 9

The hyperfine field distribution  $P(\mathbf{B}^{\text{tot}})$ , obtained by the fit of the Mössbauer reflectivity spectra and NRR curves at various values of the applied magnetic field  $\mathbf{H}^{\text{ext}}$ .

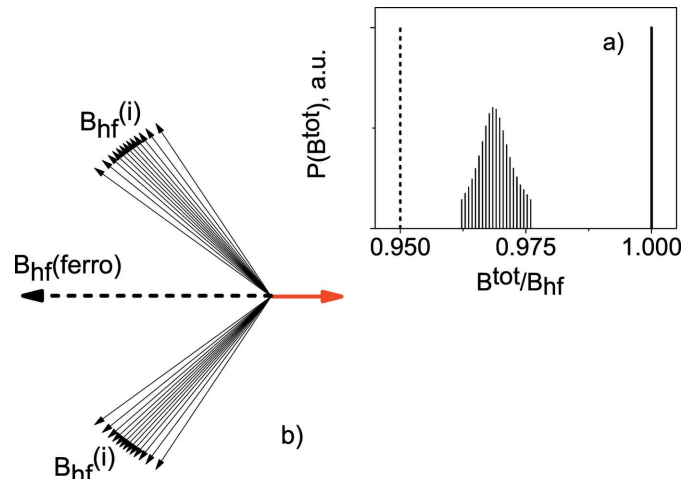


Figure 10

(a) The appearance under the action of the external field distribution of the value of the total magnetic field  $\mathbf{B}^{\text{tot}}$ , acting on the  $^{57}\text{Fe}$  nuclei  $P(\mathbf{B}^{\text{tot}})$ , if the value of  $\mathbf{B}_{\text{hf}}$  is fixed but the orientation of  $\mathbf{B}_{\text{hf}}^{(i)}$  is dispersed. The distribution  $P(\mathbf{B}^{\text{tot}})$  [the column-bar graph in (a)] is calculated for the case when  $\mathbf{B}_{\text{hf}}^{(i)}$  is oriented at a mean angle of  $135^\circ$  relative the direction of  $\mathbf{H}^{\text{ext}}$  with a Gaussian angular distribution of  $\pm 20^\circ$  [two fans of the solid black arrows in (b)]. For comparison, the solid vertical line in (a) shows the single-line distribution  $P(\mathbf{B}^{\text{tot}})$  for the case  $\mathbf{H}^{\text{ext}} = 0$  and  $\mathbf{B}^{\text{tot}} = |\mathbf{B}_{\text{hf}}|$ . The dashed vertical line in (a) is the single-line distribution  $P(\mathbf{B}^{\text{tot}})$  for the case where all  $\mathbf{B}_{\text{hf}}^{(i)} = \mathbf{B}_{\text{hf}}$  (ferro) are aligned antiparallel to  $\mathbf{H}^{\text{ext}} = 0.05|\mathbf{B}_{\text{hf}}|$  and  $\mathbf{B}^{\text{tot}} = 0.95|\mathbf{B}_{\text{hf}}|$ .

tions as those for the fit to the NRR curves and to the spectra measured near the critical angle.

The spectra show the presence of lines at the positions  $\sim \pm 3.2 \text{ mm s}^{-1}$ . In general, they would correspond to the positions of the second and fifth lines for  $\mathbf{B}_{\text{hf}}^{(i)} \simeq 33$  T. However, at the ‘magnetic’ maximum these lines could appear only if the orientation of  $\mathbf{B}_{\text{hf}}^{(i)}$  in the adjacent  $^{57}\text{Fe}$  layers is asymmetric relative to the direction of the beam, which is not confirmed by the fit. Instead, the joint fit of the reflectivity curves and of all measured spectra shows that these lines appear due to the presence in the magnetic field distribution  $P(\mathbf{B}^{\text{tot}})$  of a rather large component at  $\sim 20$  T. In other words, these lines actually are the first and sixth lines in the Mössbauer sextet for  $\mathbf{B}_{\text{hf}}^{(i)} \simeq 20$  T.

In contrast to the magnetic maximum, in the Mössbauer reflectivity spectra, measured near the critical angle, the second and fifth lines of the Mössbauer sextet for  $\mathbf{B}_{\text{hf}}^{(i)} \simeq 33$  T can contribute to the intensity of the lines near  $\sim \pm 3.2 \text{ mm s}^{-1}$  velocities. It is interesting to note that, at first glance, these lines should be more pronounced for the almost random orientation of the antiferromagnetically coupled magnetizations [top spectrum in Fig. 8(a)] than in the case of the almost ferromagnetic alignment of  $\mathbf{B}_{\text{hf}}^{(i)}$  along the beam direction [bottom left spectrum in Fig. 8(a)], where they should not be presented at all for  $\pi$ -polarized incident radiation. But, in fact, the measured spectra have the opposite trend.

The observed behavior is explained not by the increase of the second and fifth lines but by the decrease of the first, third, fourth and sixth lines in the case of ferromagnetic alignment.

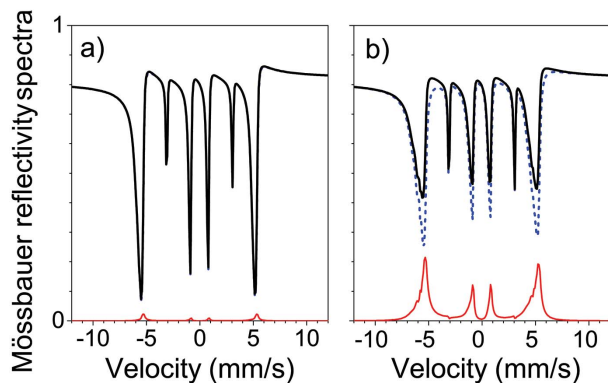


**Figure 11** Illustration of the origin of the different line ratio in the Mössbauer reflectivity spectra at  $\theta = 3.5$  mrad (slightly below the critical angle) for the antiferromagnetic (a) and ferromagnetic (b) interlayer coupling. Calculations for the  $[^{57}\text{Fe}(0.8\text{ nm})/\text{Cr}(1.05\text{ nm})]_{30}$  multilayer,  $\mathbf{B}_{\text{hf}} = 33\text{ T}$ ,  $\Delta\mathbf{B}_{\text{hf}} = 0.5\text{ T}$ , the azimuth of the  $\mathbf{B}_{\text{hf}}$  orientation is taken as  $75^\circ$ . The thick black lines show the total Mössbauer reflectivity spectra, blue dashed lines are the  $\pi \Rightarrow \pi$  reflected intensity, and thin red lines show the  $\pi \Rightarrow \sigma$  reflected intensity. The  $\pi \Rightarrow \sigma$  contribution is almost completely suppressed for the antiferromagnetic multilayer. For the ferromagnetic alignment, the  $\pi \Rightarrow \sigma$  contribution reduces the dips at the first, third, fourth and sixth line positions, which visually enlarges the second and fifth lines.

For almost ferromagnetic alignment of magnetizations in  $^{57}\text{Fe}$  layers the four lines with  $\Delta m = \pm 1$  are reduced due to the contribution of the ‘rotated’ polarization. In the region of the total reflection, the reflectivity spectrum looks similar to the absorption spectrum, *i.e.* they show the dips at the resonant energies. The contribution of the ‘rotated’ polarization to the total reflectivity is presented as peaks, and these peaks reduce the dips at the positions of the  $\Delta m = \pm 1$  lines. This behavior is illustrated in Fig. 11.

Finally, we note that the fit of the X-ray reflectivity curve (Fig. 6) has been performed prior to the rest of the data processing. This fit gives the geometrical parameters of the multilayer and the electronic densities of layers. In particular, it turns out that the period  $D$  of the structure equals  $1.587\text{ nm}$  ( $d_{\text{Fe}} = 0.636\text{ nm}$ ,  $d_{\text{Cr}} = 0.951\text{ nm}$ ), which is slightly smaller than the nominal value. The width of the interfaces is  $\sim 0.6\text{ nm}$ . Thus, the Cr and  $^{57}\text{Fe}$  layers are significantly intermixed. This conclusion follows as well from the rather broad distribution of the magnetic field  $\mathbf{B}^{\text{tot}} = |\mathbf{H}^{\text{ext}} + \sum_i \mathbf{B}_{\text{hf}}^{(i)}|$  values (Fig. 9).

## 5. Conclusions

The specific features of the Mössbauer reflectivity spectra measured for various grazing angles with a synchrotron Mössbauer source and pure  $\pi$ -polarized radiation in the conventional energy scale at different grazing angles have been thoroughly analyzed and explained.

The full set of the experimental data, obtained for the  $[\text{Fe}/\text{Cr}]_{30}$  multilayer for various values and orientations of the applied magnetic field, has been fitted by the program package *REFSPC* specially developed for this task. The magnetization profiles and hyperfine field value distributions have been

recovered for each magnitude of the applied external field. The performed Mössbauer reflectivity experiment with the SMS at the ESRF demonstrates the high efficiency of such investigations for the analysis and understanding of the multilayer structure and magnetization profiles.

The Mössbauer reflectivity experiments can give more reliable results than, for example, polarized neutron reflectivity (see, for example, te Velthuis *et al.*, 2002; Lauter-Pasyuk *et al.*, 2002; Meersschart *et al.*, 2006), because in the Mössbauer case the set of Mössbauer reflectivity spectra is measured at several grazing angles in addition to the NRR curves. The fit of the NRR curve with a large number of parameters, characterizing the magnetization depth profiles in a multilayer, is not unambiguous, but the joint fit with the Mössbauer reflectivity spectra measured near the critical angle and at the ‘magnetic’ maximum provides a plausibility of the derived models.

## Funding information

Funding for this research was provided by the Russian Federal Agency for Scientific Organizations on the theme ‘Spin’ No. 01201463330 and by the Project No. 1.1.3.5. of the Program No. 32 of the Presidium of Russian Academy of Sciences, and the research was supported in part by the Russian Foundation for Basic Research (Grants No. 15-02-01674-a, No. 15-02-01502-a and No. 16-02-00887-a).

## References

Andreeva, M. A. (1996). *Phys. Lett. A*, **210**, 359–363.  
 Andreeva, M. A. (2001). *Proc. SPIE*, **4605**, 368–373.  
 Andreeva, M. A. (2008). *Hyperfine Interact.* **185**, 17–21.  
 Andreeva, M. A. (2010). *J. Phys. Conf. Ser.* **217**, 012013.  
 Andreeva, M. A., Baulin, R. A., Chumakov, A. I., Rüffer, R., Smirnov, G. V., Babanov, Yu. A., Devyaterikov, D. I., Goloborodsky, D. Yu., Ponomarev, D. A., Romashev, L. N. & Ustinov, V. V. (2017a). *J. Magn. Magn. Mater.* **440**, 225–229.  
 Andreeva, M. A., Baulin, R. A., Chumakov, A. I., Rüffer, R., Smirnov, G. V., Babanov, Yu. A., Devyaterikov, D. I., Milyaev, M. A., Ponomarev, D. A., Romashev, L. N. & Ustinov, V. V. (2017b). arXiv:1708.06269 [cond-Mater.mes-hall].  
 Andreeva, M. A., Belozerskii, G. N., Irkaev, S. M., Semenov, V. G., Sokolov, A. Yu. & Shumilova, N. V. (1991). *Phys. Status Solidi A*, **127**, 455–464.  
 Andreeva, M. A., Chumakov, A. I., Smirnov, G. V., Babanov, Yu. A., Devyaterikov, D., Goloborodsky, B., Ponomarev, D., Romashev, L. N., Ustinov, V. V. & Rüffer, R. (2016a). *Hyperfine Interact.* **237**, 25.  
 Andreeva, M. A., Gittsovich, V. N., Irkaev, V. N. & Semenov, V. G. (1997). *Proc. SPIE*, **3239**, 412–421.  
 Andreeva, M., Gupta, A., Sharma, G., Kamali, S., Okada, K. & Yoda, Y. (2015). *Phys. Rev. B*, **92**, 134403.  
 Andreeva, M. A., Irkaev, S. M., Neplokhov, D. O., Polushkin, N. N., Salachshenko, N. N. & Semenov, V. G. (1998). *J. Surface Invest. X-ray Synchrotron Neutron Tech.* **13**, 1529–1540.  
 Andreeva, M. A., Irkaev, S. M., Semenov, V. G., Prokhorov, K. A., Salachshenko, N. N., Chumakov, A. I. & Rüffer, R. (1999). *J. Alloys Compd.* **286**, 322–332.  
 Andreeva, M. A. & Lindgren, B. (2002). *JETP Lett.* **76**, 704–706.  
 Andreeva, M. A. & Lindgren, B. (2005). *Phys. Rev. B*, **72**, 125422.

- Andreeva, M. A., Lindgren, B. & Panchuck, V. (2016b). *REFTIM*, <http://www.esrf.eu/Instrumentation/software/data-analysis/OurSoftware/REFTIM>.
- Andreeva, M. A., Monina, N. G., Lindgren, B., Häggström, L. & Kalska, B. (2007). *J. Exp. Theor. Phys.* **104**, 577–585.
- Andreeva, M. A. & Rosete, C. (1986). *Vestn. Mosk. Univ. Fiz.* **41**(3), 57–62.
- Baron, A. Q. R. (1999). *Hyperfine Interact.* **123/124**, 667–680.
- Baron, A. Q. R., Arthur, J., Ruby, S. L., Chumakov, A. I., Smirnov, G. V. & Brown, G. S. (1994). *Phys. Rev. B*, **50**, 10354–10357.
- Baron, A. Q. R., Chumakov, A. I., Grünsteudel, H. F., Grünsteudel, H., Niesen, L. & Ruffer, R. (1996). *Phys. Rev. Lett.* **77**, 4808–4811.
- Bernstein, S. & Campbell, E. C. (1963). *Phys. Rev.* **132**, 1625–1633.
- Bottyán, L., Dekoster, J., Deák, L., Baron, A. Q. R., Degroote, S., Moons, R., Nagy, D. L. & Langouche, G. (1998). *Hyperfine Interact.* **113**, 295–301.
- Catali, K., Shim, S.-H., Prakapenka, V. B., Zhao, J., Sturhahn, W., Chow, P., Xiao, Yu., Liu, H., Cynn, H. & Evans, W. J. (2010). *Earth Planet. Sci. Lett.* **289**, 68–75.
- Chumakov, A. I., Niesen, L., Nagy, D. L. & Alp, E. E. (1999). *Hyperfine Interact.* **123/124**, 427–454.
- Chumakov, A. I., Sergeev, I., Celse, J.-P., Ruffer, R., Lesourd, M., Zhang, L. & Sánchez del Río, M. (2014). *J. Synchrotron Rad.* **21**, 315–324.
- Chumakov, A. I., Smirnov, G. V., Baron, A. Q. R., Arthur, J., Brown, D. E., Ruby, S. L., Brown, G. S. & Salashchenko, N. N. (1993). *Phys. Rev. Lett.* **71**, 2489–2492.
- Couet, S., Schlage, K., Diederich, Th., Ruffer, R., Theis-Bröhl, K., Toperverg, B. P., Zhernenkov, K., Zabel, H. & Röhlberger, R. (2009). *New J. Phys.* **11**, 013038.
- Deák, L., Bayreuther, G., Bottyán, L., Gerdau, E., Korecki, J. I., Kornilov, E., Lauter, H. J., Leupold, O., Nagy, D. L., Petrenko, A. V., Pasyuk-Lauter, V. V., Reuther, H., Richter, E., Röhloberger, R. & Szilágyi, E. (1999). *J. Appl. Phys.* **85**, 1–7.
- Diederich, Th., Couet, S. & Röhlberger, R. (2007). *Phys. Rev. B*, **76**, 054401.
- Drovoisekov, A. B., Kreines, N. M., Kholin, D. I., Korolev, A. V., Milayev, M. A., Romashev, M. A. & Ustinov, V. V. (2008). *JETP Lett.* **88**, 118–122.
- Frost, J. C., Cowie, B. C. C., Chapman, S. N. & Marshall, J. F. (1985). *Appl. Phys. Lett.* **47**, 581–583.
- Gupta, A., Chakravarty, S., Rajput, P., Gupta, M. & Ruffer, R. (2008). *Hyperfine Interact.* **182**, 23–30.
- Gupta, A., Gupta, M., Chakravarty, S., Ruffer, R., Wille, H.-C. & Leupold, O. (2005). *Phys. Rev. B*, **72**, 014207.
- Gupta, A., Kumar, D., Andreeva, M. A., Gribova, A. D. & Ruffer, R. (2010). *J. Phys. Conf. Ser.* **217**, 012116.
- Irkaev, S. M., Andreeva, M. A., Semenov, V. G., Belozerskii, G. N. & Grishin, O. V. (1993a). *Nucl. Instrum. Methods Phys. Res. B*, **74**, 545–553.
- Irkaev, S. M., Andreeva, M. A., Semenov, V. G., Belozerskii, G. N. & Grishin, O. V. (1993b). *Nucl. Instrum. Methods Phys. Res. B*, **74**, 554–564.
- Irkaev, S. M., Andreeva, M. A., Semenov, V. G., Belozerskii, G. N. & Grishin, O. V. (1995). *Nucl. Instrum. Methods Phys. Res. B*, **103**, 351–358.
- Isaenko, S. A., Chumakov, A. I. & Shinkarev, S. I. (1994). *Phys. Lett. A*, **186**, 274–278.
- Kalska, B., Häggström, L., Lindgren, B., Blomquist, P., Wäppling, R., Andreeva, M. A., Nikitenko, Yu. V., Proglyado, V. V., Aksenov, V. L., Semenov, V. G., Chumakov, A. I., Leupold, O. & Ruffer, R. (2001). *Hyperfine Interact.* **136/137**, 295–300.
- Kupenko, I., McCammon, C., Sinmyo, R., Cerantola, V., Potapkin, V., Chumakov, A. I., Kantor, A., Ruffer, R. & Dubrovinsky, L. (2015). *Earth Planet. Sci. Lett.* **423**, 78–86.
- Kupenko, I., McCammon, C., Sinmyo, R., Prescher, C., Chumakov, A. I., Kantor, A., Ruffer, R. & Dubrovinsky, L. (2014). *Lithos*, **189**, 167–172.
- Lauter-Pasyuk, V., Lauter, H. J., Toperverg, B. P., Romashev, L. & Ustinov, V. V. (2002). *Phys. Rev. Lett.* **89**, 167203.
- Lindgren, B., Andreeva, M. A., Häggström, L., Kalska, B., Semenov, V. G., Chumakov, A. I., Leupold, O. & Ruffer, R. (2001). *Hyperfine Interact.* **136/137**, 439–444.
- Meersschaut, J., L'abbé, C., Almeida, F. M., Jiang, J. S., Pearson, J., Welp, U., Gierlings, M., Maletta, H. & Bader, S. D. (2006). *Phys. Rev. B*, **73**, 144428.
- Mitsui, T., Hirao, N., Ohishi, Y., Masuda, R., Nakamura, Y., Enoki, H., Sakaki, K. & Seto, M. (2009). *J. Synchrotron Rad.* **16**, 723–729.
- Mitsui, T., Seto, M., Kikuta, S., Hirao, S., Ohishi, Y., Takei, H., Kobayashi, Y., Kitao, S., Higashitaniguchi, S. & Masuda, R. (2007). *Jpn. J. Appl. Phys.* **46**, 821–825.
- Potapkin, V., Chumakov, A. I., Smirnov, G. V., Celse, J.-P., Ruffer, R., McCammon, C. & Dubrovinsky, L. (2012). *J. Synchrotron Rad.* **19**, 559–569.
- Potapkin, V., McCammon, C., Glazyrin, K., Kantor, A., Kupenko, I., Prescher, C., Sinmyo, R., Smirnov, G. V., Chumakov, A. I., Ruffer, R. & Dubrovinsky, L. (2013). *Nat. Commun.* **4**, 1427.
- Rennhofer, M., Sepiol, B., Sladeczek, M., Kmiec, D., Stankov, S., Vogl, G., Kozłowski, M., Kozubski, R., Vantomme, A., Meersschaut, A., Ruffer, R. & Gupta, A. (2006). *Phys. Rev. B*, **74**, 104301.
- Röhlberger, R. (1999). *Hyperfine Interact.* **123/124**, 301–325.
- Röhlberger, R., Bansmann, J., Senz, V., Jonas, K. L., Bettac, A., Meiwes-Broer, K. H. & Leupold, O. (2003). *Phys. Rev. B*, **67**, 245412.
- Röhlberger, R., Gerdau, E., Lüken, E., Rüter, H. D., Metge, J. & Leupold, O. (1993). *Z. Phys. B*, **92**, 489–499.
- Röhlberger, R., Thomas, H., Schlage, K., Burkell, E., Leupold, O. & Ruffer, R. (2002). *Phys. Rev. Lett.* **89**, 237201.
- Ruffer, R. & Chumakov, A. I. (1996). *Hyperfine Interact.* **97–98**, 589–604.
- Ruffer, R., Gerdau, E., Grote, M., Hollatz, R., Röhlberger, R., Rüter, H. D. & Sturhahn, W. (1991). *Nucl. Instrum. Methods Phys. Res. A*, **303**, 495–502.
- Siddons, D. P., Bergmann, U. & Hastings, U. (1993). *Phys. Rev. Lett.* **70**, 359–362.
- Siddons, D. P., Bergmann, U. & Hastings, U. (1999). *Hyperfine Interact.* **123/124**, 681–719.
- Ślęzak, T., Ślęzak, M., Zajac, M., Freindl, K., Koziol-Rachwał, A., Matlak, K., Spiridis, N., Wilgocka-Ślęzak, D., Partyka-Jankowska, E., Rennhofer, M., Chumakov, A. I., Stankov, S., Ruffer, R. & Korecki, J. (2010). *Phys. Rev. Lett.* **105**, 027206.
- Smirnov, G. V. (1999). *Hyperfine Interact.* **123/124**, 31–77.
- Smirnov, G. V. (2000). *Hyperfine Interact.* **125**, 91–112.
- Smirnov, G. V., van Bürck, U., Chumakov, A. I., Baron, A. I. & Ruffer, R. (1997). *Phys. Rev. B*, **55**, 5811–5815.
- Sturhahn, W. & Gerdau, E. (1994). *Phys. Rev. B*, **49**, 9285–9294.
- te Velthuis, S. G. E., Jiang, J. S., Bader, S. D. & Felcher, G. P. (2002). *Phys. Rev. Lett.* **89**, 127203–1–4.
- Toellner, T. L., Sturhahn, W., Röhlberger, R., Alp, E. E., Sowers, E. E. & Fullerton, E. E. (1995). *Phys. Rev. Lett.* **74**, 3475–3478.
- Trammell, G. T. & Hannon, J. P. (1978). *Phys. Rev. B*, **18**, 165–172.
- Ustinov, V. V., Romashev, L. N., Milayev, M. A., Korolev, A. V., Krinitsina, T. P. & Burkhanov, A. M. (2006). *J. Magn. Magn. Mater.* **300**, 148–152.
- Wagner, F. E. (1968). *Z. Phys. A*, **210**, 361–379.